Soil Dynamics and Earthquake Engineering 198 (2025) 109609

Contents lists available at ScienceDirect

Soil Dynamics and Earthquake Engineering

journal homepage: www.elsevier.com/locate/soildyn

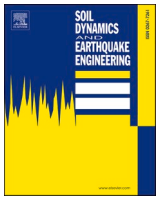

Seismic active earth pressure for bridge abutments based on design response spectrum

Haoyu Xie [a,b], Wengang Zhang [b,*], Zhaoguang Tang [c], Chuan Wei [a], Haiming Liu [a]

[a] State Key Laboratory of Bridge Safety and Resilience, China Merchants Chongqing Communication Technology R & D Institute Co., LTD., Chongqing, 400067, China
[b] School of Civil Engineering, Chongqing University, Chongqing, 400045, China
[c] Key Laboratory of Earthquake Engineering and Engineering Vibration, Institute of Engineering Mechanics, China Earthquake Administration, Harbin, 150080, China

ARTICLE INFO

Keywords:
Seismic earth pressure
Response spectrum
Power spectral density function
Pseudo-dynamic method
Centrifuge shaking table test

ABSTRACT

Calculating seismic active earth pressure for bridge abutments is a traditional yet critical issue. Existing analytical methods in the limit equilibrium state framework still have significant shortcomings in considering the time history and distribution characteristics of seismic inertial forces. Using the design response spectrum and mathematical methods derived from the random vibration theory and Fourier transform, this article proposes solutions for the horizontal seismic acceleration distribution in backfill soil. This study established a new model for calculating seismic active earth pressure for bridge abutments using the modified seismic acceleration distribution, including analytical solution formulas for the resultant force, intensity distribution, and resultant-force location. Furthermore, a series of centrifuge shaking table tests were conducted. The proposed method provided a more accurate description of the nonlinear characteristics of seismic acceleration and seismic earth pressure intensity distributions compared with conventional methods.

1. Introduction

As critical components in bridge structures, bridge abutments primarily connect a bridge deck to roadway and bear vertical loads exerted by superstructures. Thus, they can be regarded as a special type of retaining walls. Accordingly, research on seismic earth pressure acting on bridge abutments and their seismic design often relies on calculation methods for seismic earth pressure on retaining structures. These methods mainly include numerical simulation methods based on soil-structure interaction and constitutive models of backfill soil. Other methods are the Mononobe-Okabe method [1,2] (abbreviated as the M-O method and also known as the pseudo-static method), which is derived from Coulomb's earth pressure theory based on the limit equilibrium assumption, and modified analytical approaches based on the M-O method. The M-O method has been preferred for calculating lateral dynamic earth pressure in seismic design standards for bridge abutments because it provides analytical formulas for calculating seismic active and passive earth pressures, offering a natural advantage for its application in standard specifications for structural seismic design.

The pseudo-static method assumes that the backfill soil behaves as a rigid body with an infinite shear modulus and disregards the time-history characteristics of ground motion accelerations. Consequently, it fails to provide the distribution of seismic earth pressure intensity along the back of an abutment, which significantly limits its application [3]. In addition, the method employs a series of simplified assumptions regarding the dynamic characteristics of a geotechnical structure and backfill soil. To address the major limitations of conventional analytical derivations deduced based on the limit equilibrium state and further develop the theory, several representative studies based on modifications of the M-O formula have been conducted over the years. For instance, Seed and Whitman [4] conducted a parametric analysis to clarify the controlling parameters of the pseudo-static method and proposed a simplified formula based on charts. Experiments were also conducted to investigate the distribution of seismic earth pressure in different and complex conditions, and the fitted formula derived from obtained results was utilized in conjunction with the M-O formula [5–7]. Meanwhile, Wang [8] proposed the horizontal slice analysis method (HSM). In the method, the sliding soil wedge in the limit equilibrium state is divided into horizontal layers, and the distribution of earth pressure can be derived using a system of equilibrium equations. The HSM was later applied to seismic conditions [9–13]. The logarithmic spiral and its composite form assumption were suggested to replace the straight-line slip-surface assumption, establishing an improved calculation model [14,15]. The non-homogeneity and anisotropy

* Corresponding author.
E-mail address: zhangwg@cqu.edu.cn (W. Zhang).

https://doi.org/10.1016/j.soildyn.2025.109609
Received 2 March 2025; Received in revised form 12 June 2025; Accepted 12 June 2025
Available online 17 June 2025

characteristics of soils have also been incorporated in the conventional assumptions of the pseudo-static method [16,17]. Recently, the method has been utilized alongside other theories and methods to calculate seismic earth pressure, such as the upper-bound theory [18], lower-bound theory [19,20], and slip-line solution method [21].

The pseudo-dynamic method was first proposed by Steedman and Zeng [3,22], primarily to address the failure of the pseudo-static method and its modifications to consider the propagation characteristics of ground motions in backfill soil. This method presumes that backfill soil behaves as an elastic medium with a finite and depth-independent shear modulus and the seismic acceleration time history varies sinusoidally with depth and time. These considerations capture the nonlinear characteristics of seismic acceleration and earth pressure in backfill soil observed in dynamic experiments. Similar to that in case of the pseudo-static method, researches have led to various improvements in the pseudo-dynamic method, such as the inclusion of parametric analysis [23–25], assumption of diversified slip surfaces [26,27], consideration of vibration amplification effects [28,29], and combined use with other theories [30–33].

In summary, research on the limit equilibrium analysis methods for seismic earth pressure, represented by the pseudo-static and pseudo-dynamic methods, has focused mainly on the following aspects: (1) conducting parametric analysis under complex environmental conditions; (2) considering additional assumptions such as vibration amplification effects, deformation modes, and complex slip-surface configurations; (3) integrating the methods with theories, including the upper-bound theory, lower-bound theory, and wave motion theory. However, few of these studies have transcended the assumption inherent in the pseudo-dynamic method regarding the frequency-domain characteristics of ground motion acceleration; that is, the representation of seismic time-history characteristics in existing research still relies on a single parameter, the characteristic period. Therefore, existing limit equilibrium analysis methods exhibit significant limitations in representing seismic inertial forces when determining seismic earth pressure for bridge abutments. Their corresponding calculation theories and design methodologies require further development.

This study aimed to develop a more accurate prediction model for the distribution of horizontal seismic acceleration in backfill soil that includes a detailed solution and a simplified solution. The study builds on existing seismic design principles and frameworks for bridge structures and specifically leverages the design response spectrum, which is derived from the statistical analysis of a large amount of recorded seismic time-history data. Although this study acknowledges the critical roles of both active and passive conditions in the seismic stability of bridge abutments, it strategically prioritizes seismic active earth pressure given its scope constraints and direct relevance to earthquake-induced retaining wall overturning failures. By integrating theoretical analyses based on the assumption of the proposed backfill soil seismic acceleration distribution in the limit equilibrium state and centrifuge shaking table tests where the model similarity ratio is set at 50, analytical formulas for calculating seismic active earth pressures encompassing the resultant force, intensity distribution, and application location are derived.

2. Backfill soil seismic acceleration distribution

2.1. Design response spectrum

The design response spectrum sourced from the *Specifications for Seismic Design of Highway Bridges* of China [34] (Eq. (1)) was used in this study considering that it is conservative in terms of the amplification factor (set at 2.5) and the bandwidth of the control period ranging from 0 to 10 s.

$$S(T)=\begin{cases}2.5A(6T+0.4) & 0\le T<0.1\\ 2.5A & 0.1\le T<T_g\\ 2.5A(T_g/T) & T_g\le T<10\end{cases} \tag{1}$$

where A, T, T_g, and $S(T)$ denote the horizontal peak ground motion acceleration (PGA), period, characteristic period corresponding to the site category, and design response spectrum, respectively.

According to Eq. (1), the curve consists of three segments. The spectral acceleration in the ascending segment has a linear relationship with the period, the platform segment typically takes 2.5 times the PGA, and the spectral acceleration in the descending segment is a reciprocal function of the period (Fig. 1).

2.2. Power spectral density (PSD) function

To derive the acceleration distribution of backfill soil represented by the design response spectrum, its corresponding PSD function is first determined. However, there is no analytical mathematical relation between the response spectrum and PSD function. To address this, some studies [35–37] proposed approximate conversion relations between the response spectrum and the PSD function using random vibration theory, which considers the probability distribution of the maximum response of a linear system under a stationary random process input. The Kaul method [36] (Eq. (2)) is a relatively concise and practical one among these methods. Although this method may exhibit slight deviations in results at both high- and low-frequency bounds during transformation, its accuracy in the low-frequency range can be improved to a satisfactory level through damping corrections or the adoption of appropriate exceedance probability values. Meanwhile, its results in the high-frequency range inherently remain conservative, aligning with the requirement for a fail-safe PSD in seismic design [38]. Furthermore, the Kaul method has been continuously widely utilized in recent structural seismic engineering research [39,40], attesting to its reliability and relevance in modern engineering practices.

$$S_a(\omega)=\frac{2\zeta S^2(\omega)}{-\ln\{[-\pi/(\omega D)]\ln(1-r)\}\pi\omega} \tag{2}$$

where ω, $S_a(\omega)$, ζ, D, and r denote the angular frequency, the PSD function, the damping ratio, the duration of ground motion, and the exceedance probability, respectively.

With the damping ratio ζ taken as a typical value of 0.05 for reinforced concrete beam bridges and the period T transformed by the angular frequency ω, Eq. (1) is substituted into Eq. (2) to obtain the

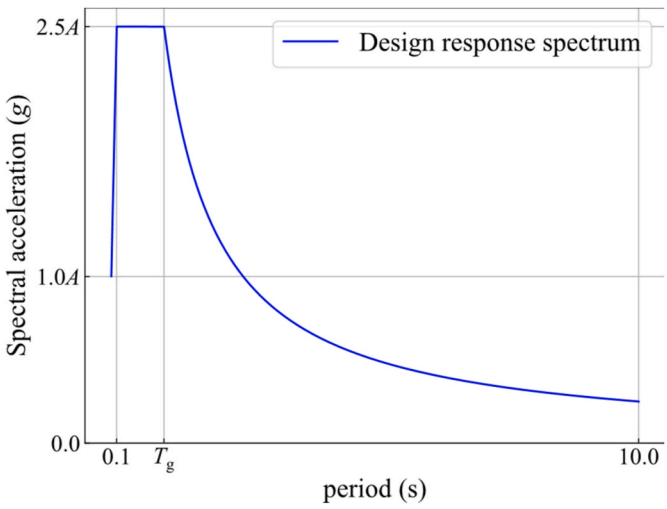

Fig. 1. Design response spectrum from the *Specifications for Seismic Design of Highway Bridges* of China.

corresponding PSD function, as expressed in Eq. (3).

$$S_a(\omega)=\begin{cases}\dfrac{0.15625T_g^2A^2\omega}{-\ln\{[-\pi/(\omega D)]\ln(1-r)\}\pi^3} & 0.2\pi\le\omega\le(2\pi/T_g)\\ \dfrac{0.625A^2}{-\ln\{[-\pi/(\omega D)]\ln(1-r)\}\pi\omega} & (2\pi/T_g)<\omega\le 20\pi\\ \dfrac{0.1A^2(30\pi/\omega+1)^2}{-\ln\{[-\pi/(\omega D)]\ln(1-r)\}\pi\omega} & 20\pi<\omega\end{cases} \quad (3)$$

Eq. (3) shows that the PSD amplitude $S_a(\omega)$ is influenced by the duration D and the exceedance probability r, while the PGA A and characteristic period T_g are artificially defined. To clarify the influence of D and r on $S_a(\omega)$, corresponding parameter analyses were conducted, with the results shown in Fig. 2.

As shown in Fig. 2 (a), increasing the duration of ground motion D decreases the PSD amplitude $S_a(\omega)$, although it has an insignificant impact on the overall trend of $S_a(\omega)$. From a structural seismic design safety perspective, it is safer to assume smaller values for D. In structural dynamic analyses, the duration of natural ground motion acceleration time histories is often taken to be relatively long, sometimes exceeding 120 s. Meanwhile, the fitted duration of artificial ground motion acceleration time histories is usually no less than 30 s for critical or long-period structures [41,42], especially given the role of the envelope function in further reducing the effective strong motion duration. Therefore, this study conservatively adopts $D=30$ s for the subsequent derivations and analyses.

As shown in Fig. 2 (b), as the exceedance probability r increases, the PSD amplitude $S_a(\omega)$ rises, but its impact on the overall trend of $S_a(\omega)$ remains insignificant. Regarding the value of r, Kaul [36] selected 0.15, which was deemed to provide highly accurate results. However, the design response spectrum is determined through statistical averaging, corresponding to the value of 0.5. Therefore, considering both structural seismic design safety and theoretical rigor, this study conservatively adopts $r=0.5$ for subsequent derivations and analyses.

2.3. Analytical solution of seismic acceleration distribution

2.3.1. Detailed solution

When calculating the magnitude and distribution of seismic acceleration in backfill soil, the inverse discrete Fourier transform and the superposition of trigonometric functions can be employed. Notably, when adopting trigonometric function superposition, the target angular frequencies involved must be real numbers. Therefore, throughout the derivation process of this study, a single-sided PSD function, which is only defined in the real frequency domain, was utilized.

The time history of ground motion acceleration corresponding to the single-sided PSD function is given by Eq. (4).

$$a(t)=\sum_{i=1}^{N}A_F(\omega_i)\sin(\omega_i t+\varphi_i) \quad (4\text{-}1)$$

$$A_F(\omega_i)=\sqrt{2S_a(\omega_i)\Delta\omega} \quad (4\text{-}2)$$

where t, ω_i, $\Delta\omega$, φ_i, $a(t)$, and $A_F(\omega_i)$ denote the time, discrete target angular frequencies, sampling interval of angular frequencies, discrete random phase angles, acceleration time history, and discrete Fourier amplitudes, respectively.

Based on the analytical model of the pseudo-dynamic method [3], the horizontal seismic acceleration in the backfill soil (propagating through shear within the soil mass) at a certain depth and time is given by Eq. (5).

$$a(z,t)=a[t-(H-z)/v_s] \quad (5\text{-}1)$$

$$v_s=\sqrt{G/\rho} \quad (5\text{-}2)$$

where $a(z,t)$, H, v_s, G, and ρ denote the acceleration time history at depth z, height of the bridge abutment, shear wave velocity, elastic modulus, and density of the backfill soil, respectively.

Eq. (4) is substituted into Eq. (5) to derive the seismic acceleration distribution based on the one-sided PSD function, as expressed in Eq. (6).

$$a(z,t)=\sum_{i=1}^{N}\sqrt{2S_a(\omega_i)\Delta\omega}\sin\{\omega_i[t-(H-z)/v_s]+\varphi_i\} \quad (6)$$

With $\Delta\omega$ set to 0.01π rad/s to satisfy the requirement of $\Delta\omega\le 2\pi/D$ in signal processing principles and other parameters set to the suggested values mentioned in Section 2.2, Eq. (7) is obtained by substituting Eq. (3) into Eq. (6) and expanding it. Thus, Eq. (7) represents a detailed solution of the seismic acceleration distribution.

$$a(z,t)=a_1(z,t)+a_2(z,t)+a_3(z,t) \quad (7\text{-}1)$$

$$a_1(z,t)=\sum_{i=1}^{N_1}\sqrt{\frac{0.003125T_g^2A^2\omega_i}{-\ln\{[-\pi/(30\omega_i)]\ln 0.5\}\pi^2}}\sin\{\omega_i[t-(H-z)/v_s]+\varphi_i\} \quad (7\text{-}2)$$

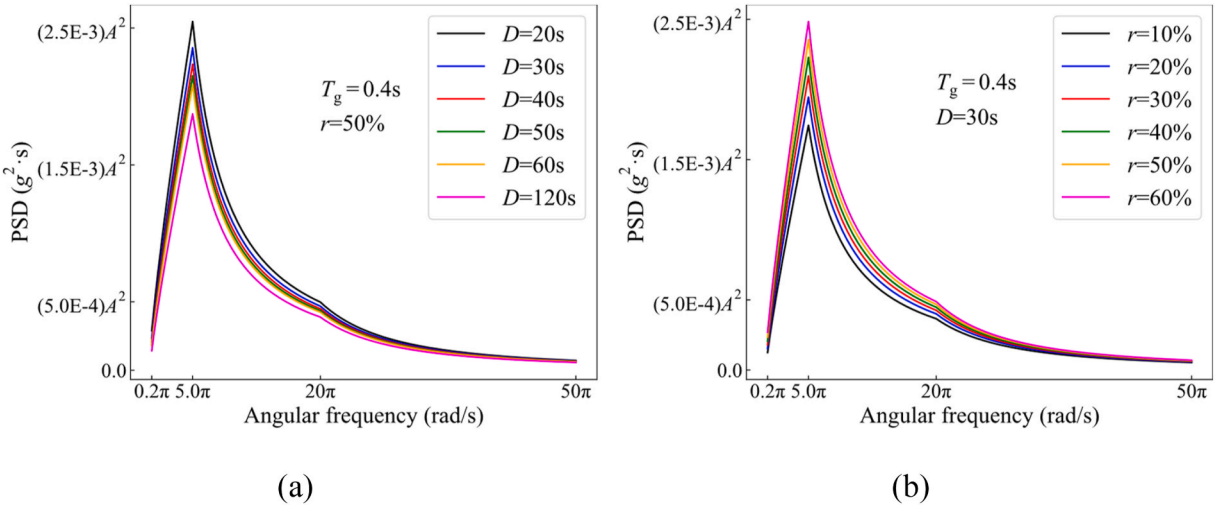

Fig. 2. Parametric analysis results: (a) influence of the duration of ground motion D on the PSD amplitude $S_a(\omega)$ and (b) influence of the exceedance probability r on the PSD amplitude $S_a(\omega)$.

$$a_2(z,t)=\sum_{i=N_1+1}^{N_2}\sqrt{\frac{0.0125A^2}{-\ln\{[-\pi/(30\omega_i)]\ln 0.5\}\omega_i}}\sin\{\omega_i[t-(H-z)/v_s]+\varphi_i\} \tag{7-3}$$

$$a_3(z,t)=\sum_{i=N_2+1}^{N_3}\sqrt{\frac{0.0125A^2(12\pi/\omega_i+0.4)^2}{-\ln\{[-\pi/(30\omega_i)]\ln 0.5\}\omega_i}}\sin\{\omega_i[t-(H-z)/v_s]+\varphi_i\} \tag{7-4}$$

where N_1, N_2, and N_3 denote the number of sampling points within certain intervals of the corresponding PSD.

2.3.2. Simplified solution

As detailed in Section 2.3.1, the magnitude and distribution of seismic acceleration in the backfill soil behind the bridge abutment can feasibly be calculated under random seismic excitations with arbitrary frequency-domain characteristics. However, Eq. (7) involves the summation of a complex series for which no general formula is available, complicating subsequent analytical derivations for seismic earth pressures. Therefore, a simplified solution is proposed by selecting characteristic angular frequencies from the detailed solution as control frequencies and assigning an equal value to the random phase spectrum to ensure that the amplitude of the stationary Gaussian process reaches its theoretical limit.

In the simplified solution, the characteristic angular frequencies ω_1, ω_2, ω_3, ω_4, and ω_5 are selected. The frequencies $\omega_1 = 0.2\pi$ rad/s and $\omega_5 = 50\pi$ rad/s are selected to bound the PSD's effective range to the design response spectrum's period limits: 10 s and near 0 s (non-closed interval), respectively. The results of an energy analysis using Parseval's theorem are shown in Table 1, which confirm minimal marginal gains from only 0.9 % to 1.9 % when adopting higher ω_5 values from 75π rad/s to 150π rad/s. This justifies $\omega_5 = 50\pi$ rad/s as a sufficiently representative value for capturing the frequency-domain energy content. The dominant frequencies $\omega_3 = \omega_{ch}$ (characteristic angular frequency) and $\omega_4 = 20\pi$ rad/s align with PSD peaks, as shown in Fig. 2, which are mapped to the design response spectrum's characteristic period T_g and the 0.1 s period. The intermediate frequency $\omega_2 = \omega_{ch}/5$ is inserted between ω_1 and ω_3 as this certain band is the most energy-dense PSD region, as shown in Fig. 2, and coincides with the nonlinear amplitude variation zone of the design response spectrum. This valuation follows classical practices where $5T_g$ is often adopted as a control period in acceleration response spectra used for bridge design [43].

Specific selections of characteristic angular frequencies are presented in Table 2.

By substituting the values of ω_i, $\Delta\omega_i$ and φ_i from Table 2 and the recommended D and r values from Section 2.2's parametric analysis into Eq. (3), the resulting expression is then substituted into Eq. (6). This is followed by the normalization of the trigonometric time-series coefficients at selected frequencies to ensure amplitude consistency. Finally, the algebraic decomposition of the normalized formulation yields the explicit form of Eq. (8).

$$a(z,t)=\sum_{i=1}^{5}k_iA\cos\{\omega_i[t-(H-z)/v_s]\} \tag{8-1}$$

$$k_i=\kappa_i/(\kappa_1+\kappa_2+\kappa_3+\kappa_4+\kappa_5) \tag{8-2}$$

Table 1
Total spectral energy for different PSD upper bounds.

PSD upper bound (rad/s)	Total spectral energy (g^2•s)	Normalized energy
50π	$0.0261A^2$	1.000
75π	$0.0264A^2$	1.009
100π	$0.0265A^2$	1.013
125π	$0.0266A^2$	1.017
150π	$0.0267A^2$	1.019

Table 2
Valuation of the characteristic control points in the frequency domain for the simplified solution.

Angular frequency of control points (rad/s)	Period of control points	Bandwidth (interval) of control points	Phase angle of control points
$\omega_1 = 0.2\pi$	$T_1 = 10$ s	$\Delta\omega_1 = (\omega_2 - \omega_1)/2$	$\varphi_1 = \pi/2$
$\omega_2 = \omega_{ch}/5$	$T_2 = 5T_g$	$\Delta\omega_2 = (\omega_3 - \omega_1)/2$	$\varphi_2 = \pi/2$
$\omega_3 = \omega_{ch}$	$T_3 = T_g$	$\Delta\omega_3 = (\omega_4 - \omega_2)/2$	$\varphi_3 = \pi/2$
$\omega_4 = 20\pi$	$T_4 = 0.1$ s	$\Delta\omega_4 = (\omega_5 - \omega_3)/2$	$\varphi_4 = \pi/2$
$\omega_5 = 50\pi$	$T_5 = 0.04$ s	$\Delta\omega_5 = (\omega_5 - \omega_4)/2$	$\varphi_5 = \pi/2$

Note: T_1-T_5, $\Delta\omega_1$-$\Delta\omega_5$, and φ_1-φ_5 denote the periods, bandwidths, and phase angles corresponding to the control angular frequencies ω_1-ω_5, respectively; ω_{ch} denotes the characteristic angular frequency corresponding to the characteristic period T_g.

$$\kappa_1=\sqrt{(\omega_{ch}-\pi)/\{40[\ln 6-\ln(\ln 2)]\omega_{ch}^2\}} \tag{8-3}$$

$$\kappa_2=\sqrt{(5\omega_{ch}-\pi)/\{40\pi[\ln\omega_{ch}+\ln 6-\ln\pi-\ln(\ln 2)]\omega_{ch}\}} \tag{8-4}$$

$$\kappa_3=\sqrt{(100\pi-\omega_{ch})/\{8\pi[\ln\omega_{ch}+\ln 30-\ln\pi-\ln(\ln 2)]\omega_{ch}\}} \tag{8-5}$$

$$\kappa_4=\sqrt{(50\pi-\omega_{ch})/\{32\pi^2[\ln 600-\ln(\ln 2)]\}} \tag{8-6}$$

$$\kappa_5=\sqrt{96/\{625\pi[\ln 1500-\ln(\ln 2)]\}} \tag{8-7}$$

where κ_i and k_i respectively denote the coefficients of the trigonometric time-series before and after the normalization, corresponding to the control angular frequencies ω_i.

The normalized coefficients k_i arise from ensuring that the sum of κ_i equals unity to maintain consistency between the assumed PGA and the derived acceleration amplitude A. This normalization corrects for the mathematical approximation inherent in converting a response spectrum to a PSD by the Kaul method, where non-normalized κ_i would possibly violate the PGA boundary condition.

To elucidate the influence of the characteristic angular frequency ω_{ch} on the amplitude coefficients k_1 to k_5, their variation trends for selected ω_{ch} values are presented in Fig. 3.

As shown in Fig. 3, k_3 and k_4 are significantly larger than the other coefficients, indicating that the influences of ω_3 (corresponding to the characteristic period) and ω_4 (corresponding to the period of 0.1 s) are the most prominent in the proposed acceleration distribution and reflecting the overall and widespread influence of the platform segment

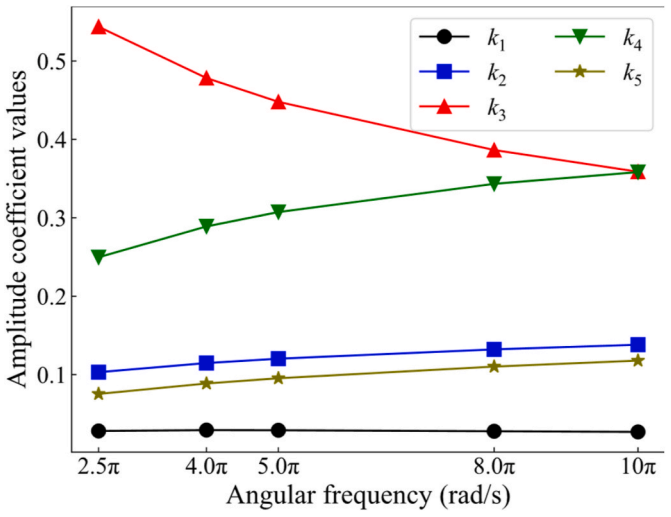

Fig. 3. Variation trends of the amplitude coefficients for the characteristic angular frequency.

from the design response spectrum. This differs from the assumption in the pseudo-dynamic method, which posits direct influence solely from the characteristic period. Moreover, as the characteristic angular frequency increases, k_3 gradually decreases while k_4 rises. This trend is attributed to the narrowing of the bandwidth corresponding to ω_3 as the characteristic period shortens.

2.3.3. Comparison of acceleration distribution models

Fig. 4 compares the assumed acceleration distributions on backfill soil between the proposed simplified solution and the pseudo-dynamic method under different shear wave velocities v_s and characteristic periods T_g when PGA is reached at the top of the abutment.

As shown in Fig. 4, the backfill soil seismic acceleration distribution calculated using the proposed simplified solution is enveloped by the distribution assumed in the pseudo-dynamic method under varying v_s and T_g conditions. Notably, the proposed solution exhibits more pronounced nonlinear distribution characteristics, which gradually diminish as v_s increases.

3. Seismic active earth pressure

3.1. Assumptions and the analytical model

The analytical model for seismic active earth pressure derived in this study was primarily based on the fundamental assumptions of the pseudo-dynamic method [3,32], with additional novel assumptions. The assumptions were simplified to focus the derivation of seismic active earth pressure on the proposed simplified solution of seismic acceleration distribution mentioned in Section 2.3.2. The assumptions were as follows:

(1) The backfill soil behind the bridge abutment is homogeneous and isotropic, with a constant shear modulus along its height.
(2) Regarding the dynamic characteristics of the backfill soil, the derivation does not consider cohesion and vibration amplification effects.
(3) Regarding the engineering and mechanical conditions considered in the analytical model, the derivation does not account for the slope of the backfill soil, surcharge loads on the backfill soil, and vertical seismic effects.
(4) The slip surface in the sliding soil wedge in the analytical model is assumed to be a straight line (plane), considering the core research objective and reduced significance of complex slip-surface geometries under active earth pressure conditions [44].
(5) Seismic acceleration distribution proposed in Section 2.3.2 and expressed in Eq. (8) is used to calculate the seismic inertial force in the analytical model.

These simplifications, particularly regarding soil amplification, vertical ground motion effects, and planar slip assumption, highlight current model limitations while paving the way for more comprehensive analyses in future investigations.

Given the above assumptions, an analytical model of seismic active earth pressure for bridge abutments in the limit equilibrium state was established, as shown in Fig. 5. In this model, P_{ae}, Q, W, and R denote the resultant force of seismic active earth pressure, seismic inertial force, gravitational inertial force, and resistance force beneath, respectively. Meanwhile, H, z, α, θ, δ, and φ denote the bridge abutment height, depth of the backfill soil, angle between the abutment back and vertical direction, slip angle of the soil wedge, friction angle between the abutment and backfill soil, and internal friction angle of the backfill soil, respectively.

3.2. Derivation of analytical formulas

3.2.1. Resultant force

Using the analytical model shown in Fig. 5, the horizontal equilibrium equation and the vertical equilibrium equation for the sliding soil wedge were determined, as shown in Eq. (9-1) and Eq. (9-2), respectively.

$$Q+\sin(\theta-\varphi)R=\cos(\alpha+\delta)P_{ae} \tag{9-1}$$

$$W=\cos(\theta-\varphi)R+\sin(\alpha+\delta)P_{ae} \tag{9-2}$$

Using the cosine formula for the difference of two angles and eliminating the resistance force beneath the soil wedge R through the system of equations, the resultant force of seismic active earth pressure P_{ae} was derived, as expressed in Eq. (10).

$$P_{ae}=\frac{\cos(\theta-\varphi)Q+\sin(\theta-\varphi)W}{\cos(\alpha+\delta+\varphi+\theta)} \tag{10}$$

According to their respective definitions, the seismic inertial force Q and gravitational inertial force W are derived using Eq. (11) and Eq. (12).

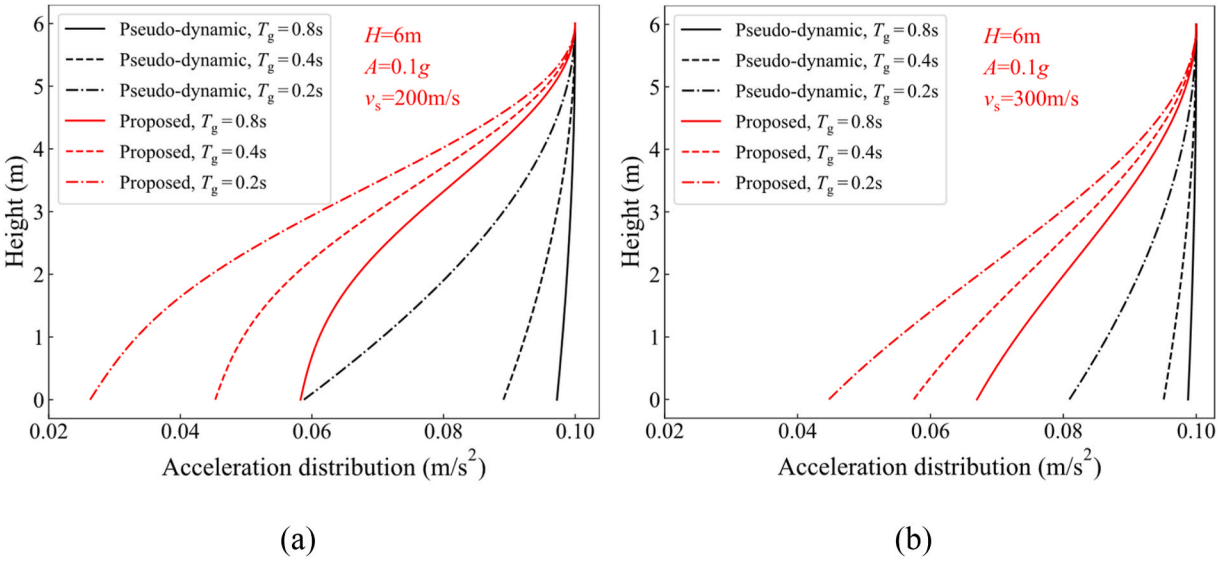

Fig. 4. Comparison of acceleration distributions v_s at (a) 200 m/s and (b) 300 m/s.

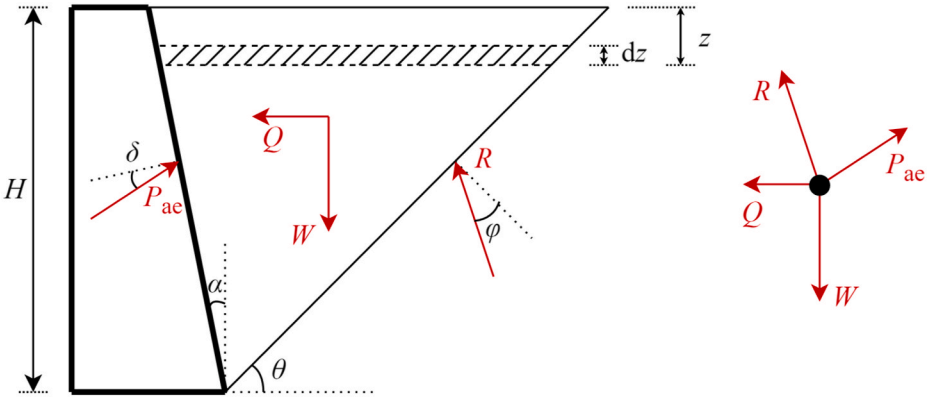

Fig. 5. Analytical model for seismic active earth pressure.

$$Q(t)=\int_0^H (\gamma/g)[(H-z)/\tan\theta]a(z,t)\mathrm{d}z \tag{11}$$

where γ and g denote the unit weight of the backfill soil and gravitational acceleration, respectively.

$$W=0.5\gamma H^2(\tan\alpha+\cot\theta) \tag{12}$$

Eq. (9)–(12) were derived from the analytical model illustrated in Fig. 5. These equations share foundational principles with classical methodologies established in prior studies [3,22,23].

By substituting Eq. (8-1) into Eq. (11), Q is obtained under the proposed seismic acceleration distribution of the backfill soil, as expressed in Eq. (13).

$$Q(t)=\int_0^H (\gamma/g)[(H-z)/\tan\theta]\sum_{i=1}^{5}k_iA\cos\{\omega_i[t-(H-z)/v_s]\}\mathrm{d}z \tag{13}$$

By solving the definite integral expressed in Eq. (13), the analytical solution for Q is obtained, as given by Eq. (14).

$$Q(t)=\frac{\gamma A(\tan\alpha+\cot\theta)v_s}{g}\sum_{i=1}^{5}\frac{k_i}{\omega_i}\left[\frac{v_s\cos(\omega_i\mu)}{\omega_i}-H\sin(\omega_i\mu)-\frac{v_s\cos(\omega_i t)}{\omega_i}\right] \tag{14-1}$$

$$\mu=t-H/v_s \tag{14-2}$$

Using Eq. (8-2)–(8-7), the amplitude coefficients corresponding to the trigonometric acceleration time-series are calculated. The coefficients k_1–k_5 are then substituted into Eq. (14). Subsequently, by substituting Eq. (14) and Eq. (12) into Eq. (10), the resultant force of the seismic active earth pressure on bridge abutments (P_{ae}) is finally obtained.

3.2.2. Intensity distribution

By substituting the variable depth z for the constant abutment height H in Eq. (10), (12) and (14), $P_{ae}(z,t)$ is defined as the resultant seismic active earth pressure force acting on the abutment section from the top surface to depth z. Subsequently, taking the partial derivative of $P_{ae}(z,t)$ with respect to z derives the distribution of seismic active earth pressure intensity through the proposed methodology, as expressed in Eq. (15).

$$p_{ae}(z,t)=\partial P_{ae}(z,t)/\partial z=p_{ae,s}(z,t)+p_{ae,d}(z,t) \tag{15-1}$$

$$p_{ae,s}(z,t)=\gamma z\sin(\theta-\varphi)(\tan\alpha+\cot\theta)/\cos(\alpha+\delta+\varphi-\theta) \tag{15-2}$$

$$p_{ae,d}(z,t)=\frac{A\gamma z\cos(\theta-\varphi)(\tan\alpha+\cot\theta)}{g\cos(\alpha+\delta+\varphi-\theta)}\sum_{i=1}^{5}k_i\cos\left[\omega_i\left(t-\frac{z}{v_s}\right)\right] \tag{15-3}$$

where $p_{ae}(z,t)$, $p_{ae,s}(z,t)$, and $p_{ae,d}(z,t)$ denote the seismic active earth pressure intensity distribution, its static component, and its dynamic component, respectively.

As shown in Eq. (15), the static component $p_{ae,s}(z,t)$ is equal to the Coulomb active earth pressure and is independent of the corresponding time-history characteristics. Meanwhile, the dynamic component $p_{ae,d}(z,t)$ shares its form with the dynamic component in the pseudo-dynamic method, with the sole distinction lying in the consideration of seismic acceleration distribution. When $t=0$ s and v_s approaches infinity, the result of $p_{ae}(z,t)$ in Eq. (15) converges to that of the pseudo-static method, consistent with the pseudo-dynamic method.

3.2.3. Location of the resultant force

For the analytical model shown in Fig. 5, the equilibrium equation of the seismic active earth pressure moment for the sliding soil wedge rotating about the base of the bridge abutment is established in Eq. (16).

$$P_{ae}(t)H_d=\int_0^H (H-z)p_{ae}(z,t)\mathrm{d}t \tag{16}$$

where H_d denotes the height of the location of the resultant force relative to the base of the bridge abutment.

By substituting the analytical solution of $p_{ae}(z,t)$ detailed in Section 3.2.2 into Eq. (16) and expanding it, the analytical solution of the definite integral in Eq. (16) is obtained, as expressed in Eq. (17).

$$Y(z,t)=\frac{\gamma(\tan\alpha+\cot\theta)}{\cos(\alpha+\delta+\varphi-\theta)}\left[\sin(\theta-\varphi)Y_s(z,t)+\frac{A}{g}\cos(\theta-\varphi)Y_d(z,t)\right] \tag{17-1}$$

$$Y_s(z,t)=H^3/6 \tag{17-2}$$

$$Y_d(z,t)=\sum_{i=1}^{5}\frac{10v_s^2k_i}{\omega_i\pi^2}\left[\frac{2\pi}{\omega_i}v_s\sin\left(\frac{\omega_iH}{2v_s}\right)-5\omega_iH\cos\left(\frac{\omega_iH}{2v_s}\right)\right]\cos\left[\frac{\omega_i(H-2tv_s)}{2v_s}\right] \tag{17-3}$$

where $Y_s(z,t)$ and $Y_d(z,t)$ represent the static and dynamic components of the analytical solution $Y(z,t)$ of the definite integral expressed as Eq. (16), respectively.

The location of the resultant force of seismic active earth pressure (H_d) is thus derived by substituting the analytical solution of $P_{ae}(t)$ detailed in Section 3.2.1 and Eq. (17) into Eq. (16).

Fig. 6 illustrates a step-by-step flowchart visually summarizing the entire analytical derivation process, from the design response spectrum input to the seismic earth pressure output, while synthesizing the methodologies presented in Sections 2.1 through 3.2.

3.3. Parametric analysis

3.3.1. Horizontal PGA

The influence of horizontal PGA A on the proposed method for

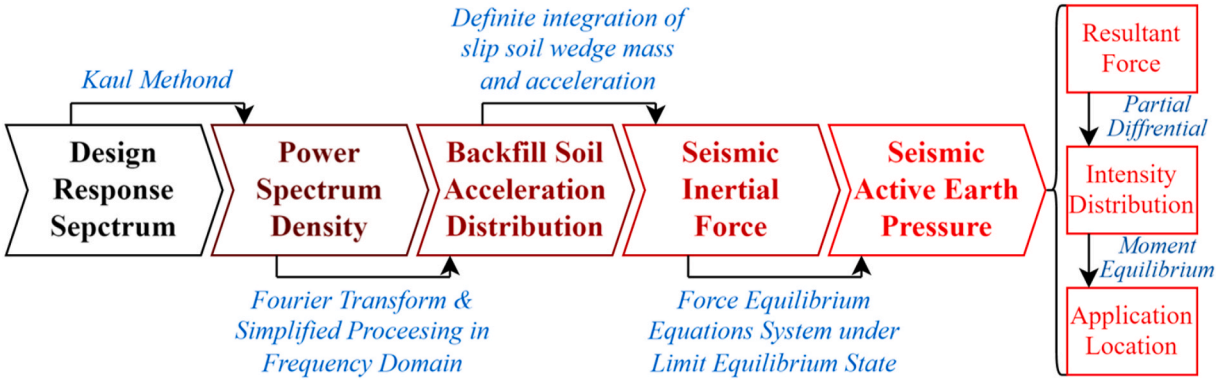

Fig. 6. Step-by-step flowchart of the analytical derivation process.

calculating seismic active earth pressure for bridge abutments is illustrated in Fig. 7, where t_{max} denotes the time at which the resultant seismic active earth pressure reaches its maximum under different conditions.

As shown in Fig. 7, the resultant force $P_{ae}(t=t_{max})$ increases nearly linearly with PGA A and is positively correlated with the abutment back angle α, indicating the advantage of downward-sloping abutments in terms of seismic design safety. Furthermore, at a specified time instant, the intensity distribution $p_{ae}(t=0,z)$ exhibits stronger nonlinear characteristics as PGA increases. Notably, the location of the maximum pressure intensity does not necessarily occur at the base of the bridge abutment.

3.3.2. Characteristic period

The influence of the characteristic period T_g on the proposed method for calculating seismic active earth pressure for bridge abutments is illustrated in Fig. 8.

As shown in Fig. 8, both the resultant force P_{ae} and the intensity distribution p_{ae} gradually increase as the characteristic period T_g becomes longer. The slope of the increase in P_{ae} gradually decreases, consistent with the pattern observed in p_{ae} where the degree of nonlinearity diminishes. From a theoretical analysis perspective, this coincides with the decrease in the diversity of acceleration distributions in backfill soil as T_g extends, as predicted by Eq. (8). Ultimately, the calculation result approaches that obtained using the M-O method.

3.4. Practical implication

This article presents a modified model for calculating seismic active earth pressure based on limit state equilibrium analysis and the pseudo-dynamic method framework. From a practical engineering perspective, the computational framework comprises three key components: the determination of seismic design parameters, identification of engineering parameters, and workflow establishment of seismic active earth pressure calculation. Although the derivation process presented herein involves frequency-domain analyses, all final expressions are presented as closed-form analytical solutions, eliminating the need for numerical integration or extensive series summation.

Simplified design charts for practical application are presented in Fig. 9, enabling the direct implementation of the proposed method in code-compliant seismic design workflows while preserving theoretical rigor.

4. Centrifuge shaking table tests

4.1. Experimental design and setup

4.1.1. Experimental equipment

Based on the experimental objectives, the DCIEM-40-300 centrifuge shaking table system (Fig. 10) provided by the Institute of Engineering Mechanics, China Earthquake Administration, was used for centrifuge shaking table tests. The main system specifications include a rotating

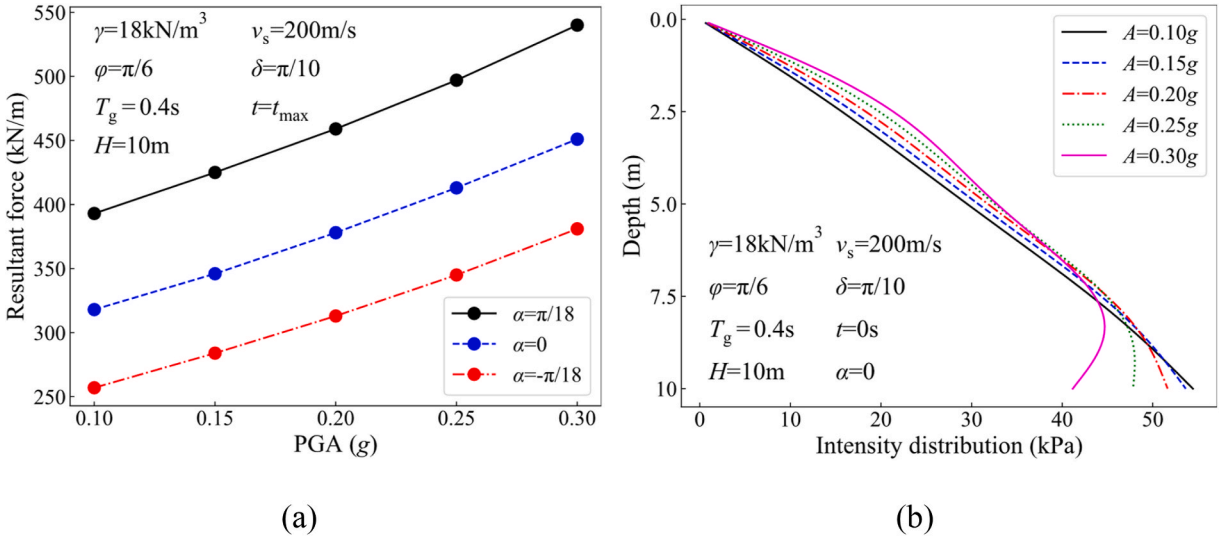

Fig. 7. Parametric analysis of the influence of PGA A on (a) the resultant force of seismic active earth pressure P_{ae} and (b) the intensity distribution of seismic active earth pressure p_{ae}.

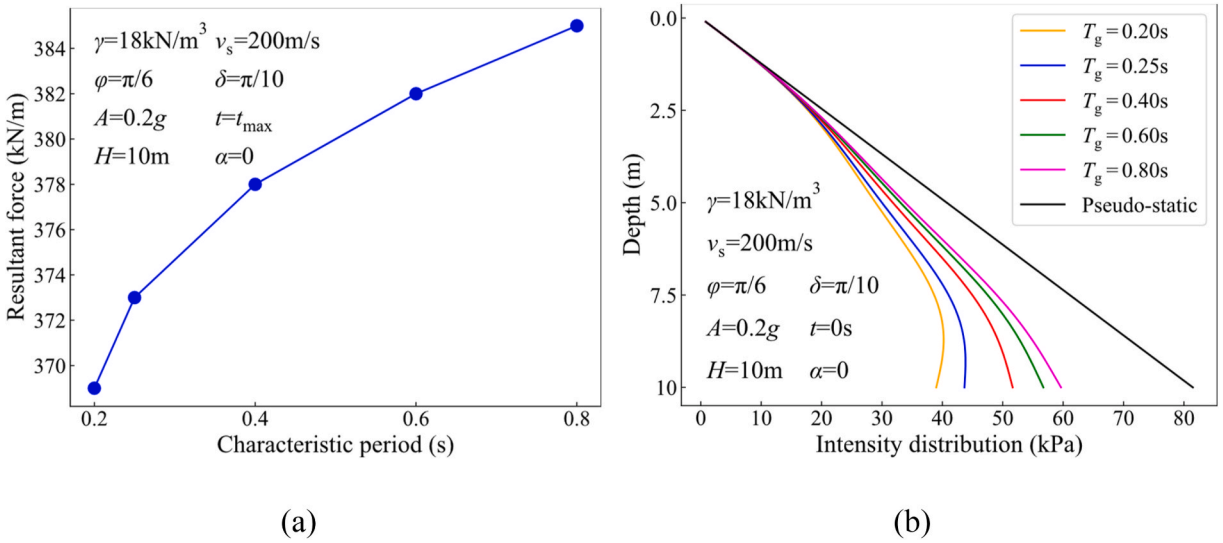

Fig. 8. Parametric analysis of the influence of the characteristic period T_g on (a) the resultant force of seismic active earth pressure P_{ae} and (b) the intensity distribution of seismic active earth pressure p_{ae}.

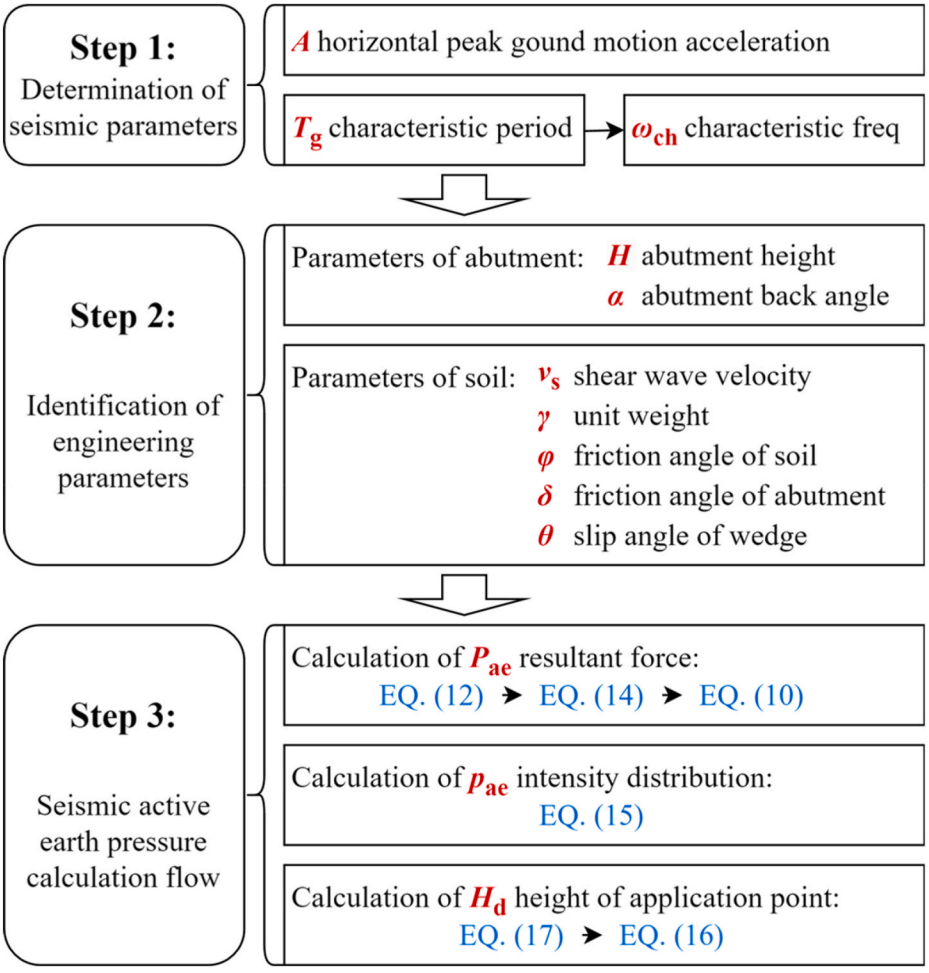

Fig. 9. Simplified design charts of the proposed analytical model.

arm radius of 5.0 m, centrifugal acceleration of 100*g*, shaking table acceleration of 30*g*, frequency range of 10–300 Hz, and vibration load capacity of 1.5 t. The Laminar Box-I type laminar shear model box (Fig. 10) was utilized, with internal dimensions of 1.2 m in length, 0.5 m in width, and 0.6 m in height. In addition, the experimental setup also included ICP-type miniature acceleration sensors, LVDT rod-type displacement sensors, and piezoresistive soft-contact soil pressure sensors.

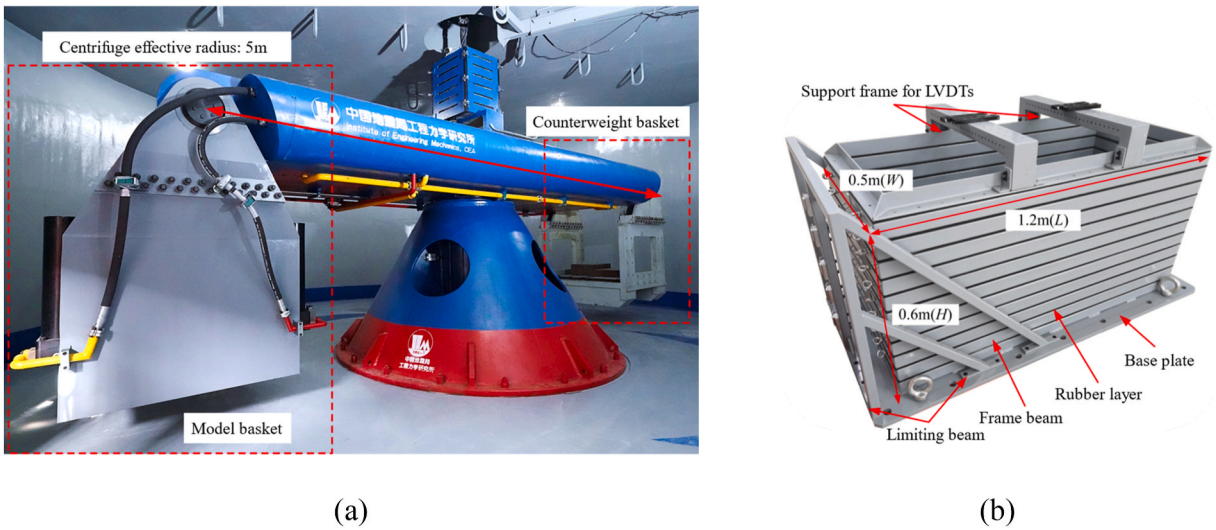

Fig. 10. Main components of the centrifuge shaking table test: (a) centrifuge shaking table system and (b) laminar shear model box.

4.1.2. Model design and sensor arrangement

The centrifugal acceleration value in the hypergravity experiment was set to 50*g*. The similarity coefficients for the main physical quantities are shown in Table 3.

Three abutment models were designed with variable inclination angles α of the abutment back, simulating vertical ($\alpha = 0$), downward-sloping ($\alpha \approx -0.15\pi$), and upward-sloping ($\alpha \approx 0.15\pi$) abutment backs, respectively. The prototype height of the abutment was 10 m, and the model height was 0.2 m based on the similarity law. The 6061 aluminum alloy, with an elastic modulus of 68.9 GPa and Poisson's ratio of 0.33, similar to those of a reinforced concrete structure, was utilized as the material for the scaled model. Three abutment models were placed in parallel within the test box. The backfill soil behind the test surfaces was Fujian standard quartz fine sand, whereas the bearing layer consisted of coarse sand.

Dynamic earth pressure sensors, acceleration sensors, and displacement sensors were utilized in the experiment. The dynamic earth pressure sensors were used to measure the resultant force and determine the intensity distribution of seismic earth pressures exerted on the models. The sensors were arranged in two columns evenly distributed along the back of each of the three abutment models, with seven sensors vertically aligned on each model. Meanwhile, the acceleration sensors were primarily utilized to monitor the seismic acceleration distribution of the backfill soil in the near-model field and the free field within the test box under seismic excitation. They were evenly distributed vertically in two sections located 130 and 680 mm from the abutment backfill. The displacement sensors were utilized to monitor the residual displacements of the three abutment models and the settlement of the backfill soil under different testing conditions.

The model dimensions, layout, and sensor arrangement are shown in Fig. 11.

Table 3
Similarity coefficients of the main physical quantities.

Category of physical quantities	Physical quantity	Design similarity coefficient
Material properties	Stress σ	1
	Strain ε	1
	Elastic modulus G	1
Geometric properties	Length l	1/50
Dynamic properties	Displacement d	1/50
	Velocity v	1
	Acceleration a	50
	Time t	1/50
	Period T	1/50
	Frequency f	50
	Stiffness k	1/50

4.1.3. Soil property

The soil types selected for experiments were Fujian standard quartz fine sand and coarse sand. For the fine sand, the gradation curve obtained through sieve analysis by layers is shown in Fig. 12. Based on this curve, the coefficient of uniformity C_u was calculated to be 1.670 and the coefficient of curvature C_c was calculated to be 0.965.

Using the vibration hammer method, funnel method, and graduated cylinder method, the maximum and minimum dry densities of the fine sand ($\rho_{d\max}$ and $\rho_{d\min}$) were determined to be 1.608 and 1.400 g/cm^3, respectively. Based on the aforementioned data and drop test results, the mass of fine sand required for the model box was calculated in accordance with the required relative density.

4.1.4. Scenario design

Three seismic acceleration time histories were considered in the experiments: that corresponding to the El-Centro wave, a specific time history from the Chichi earthquake, and that of a design-response-compatible artificial wave. The response spectra at a PGA of 1.0*g* are presented in Fig. 13.

In the experiments, the PGA values of the seismic inputs were set to 0.1*g* and 0.2*g*. Original time histories were linearly scaled to these levels, resulting in a total of six scenarios. These scenarios were ranked in ascending order according to the energy content of the seismic inputs in the frequency domain. A frequency sweep was conducted between ground motion scenarios to identify the potential plastic and residual deformations of the model system.

4.2. Results and discussions of acceleration distribution

Time-history data recorded by three acceleration sensors located in the fine sand layer of the near-model field were selected from the experimental data. These data were divided according to their corresponding elevation-based acceleration amplification factors to eliminate the influence of vibration amplification, which was not considered in the analytical model. The experimental data and acceleration distributions predicted by the proposed method of Eq. (8) and the pseudo-dynamic method are compared in Fig. 14. Specifically, the time instant t of the experimental data was chosen when the acceleration recorded by the sensor at the top of the near-model field reached its maximum acceleration, corresponding to $t = h/v_s$ in the proposed method and $t = h/v_s$ with the initial phase taken as $\pi/2$ in the pseudo-dynamic method, where h denotes the height of a certain sensor.

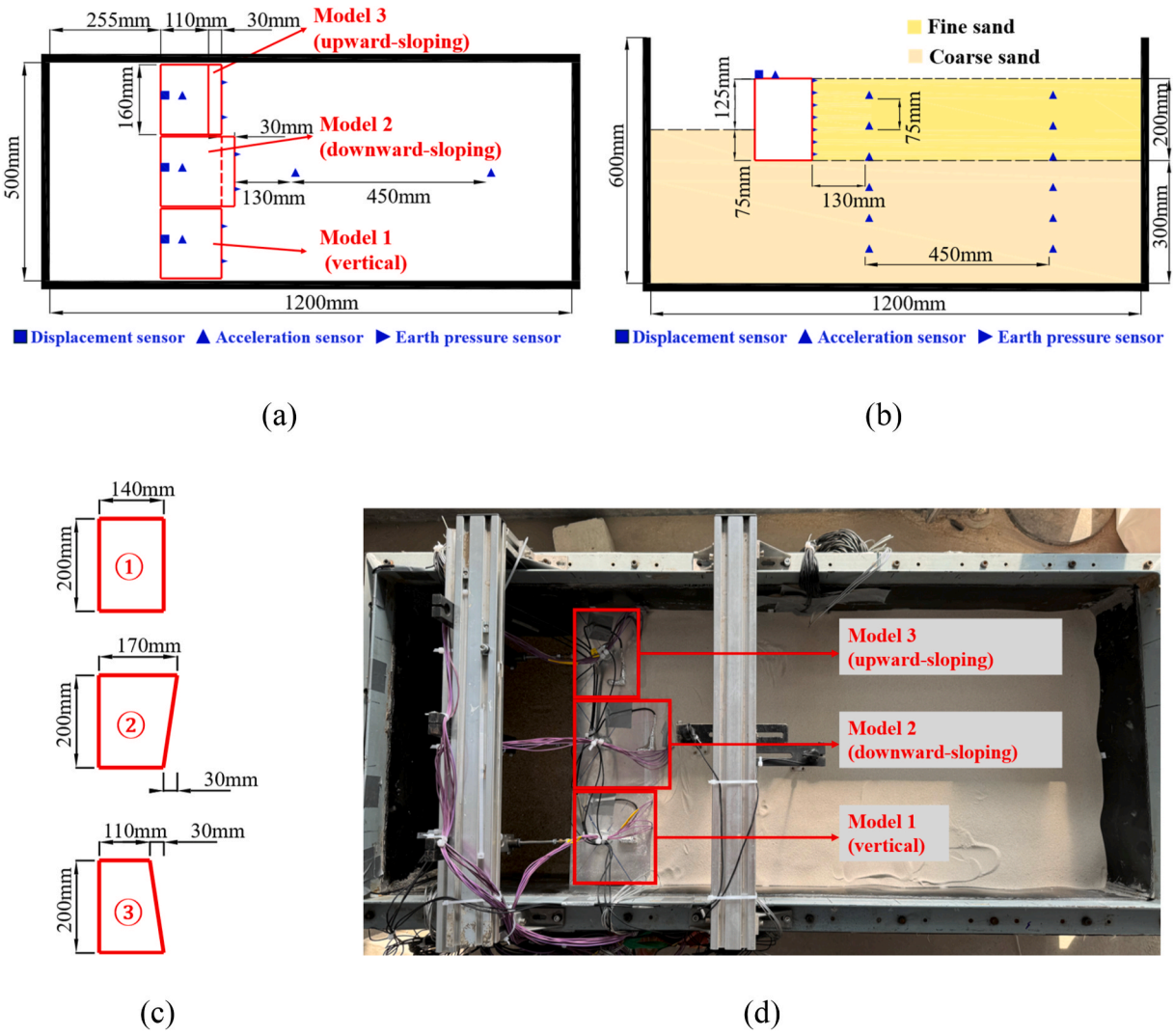

Fig. 11. Model layout and sensor arrangement: (a) schematic top view of the test box layout, (b) schematic side view of the test box layout, (c) dimensions of the models, and (d) top-view photograph of the test box layout.

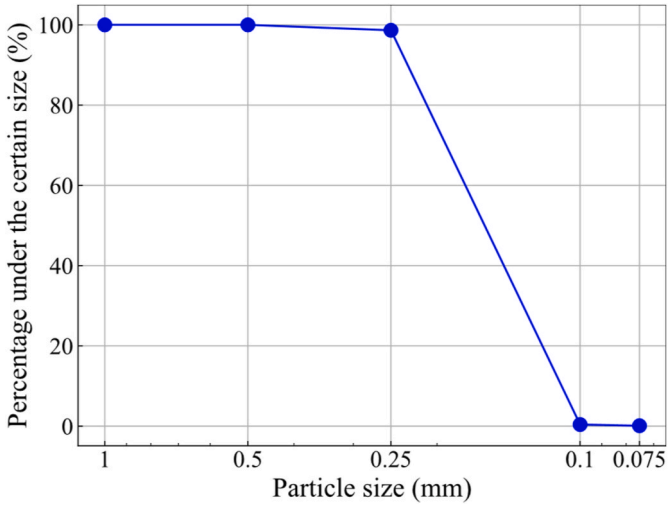

Fig. 12. Gradation curve of Fujian standard quartz fine sand.

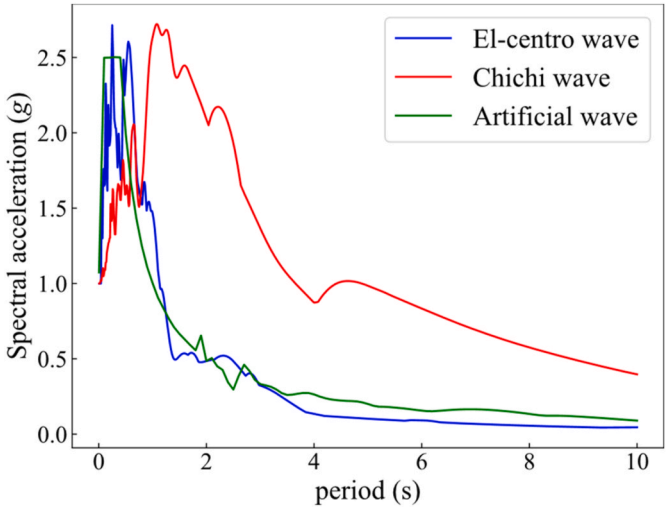

Fig. 13. Response spectra for seismic inputs.

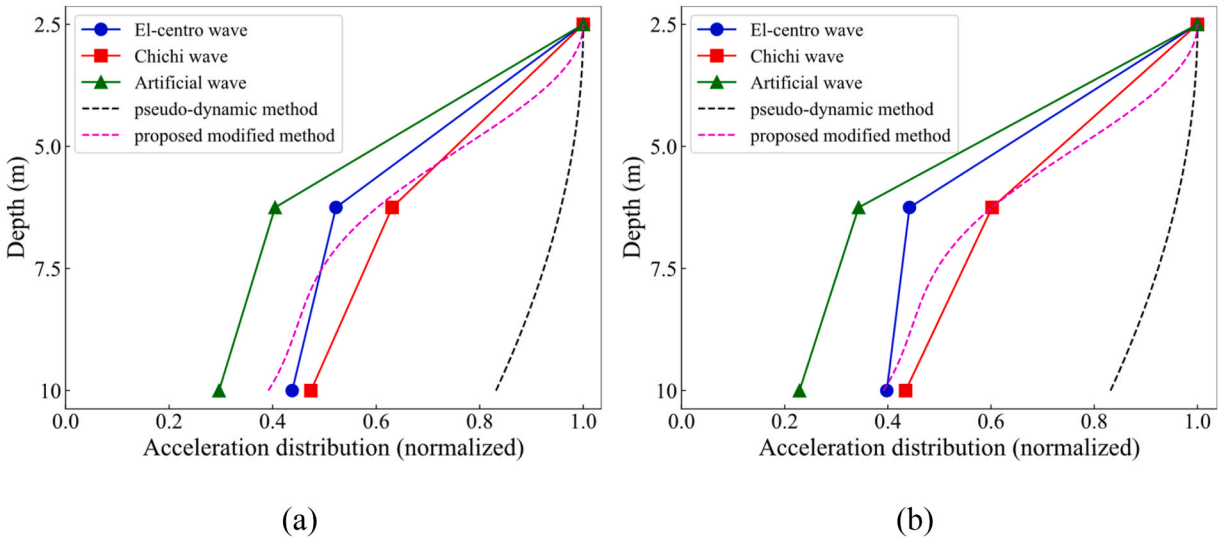

Fig. 14. Comparison of acceleration distributions at a PGA of (a) 0.1*g* and (b) 0.2*g*.

As shown in Fig. 14, the acceleration distribution calculated using the proposed method had significantly smaller deviations from the experimental data than the assumptions made by the pseudo-dynamic method. In particular, the proposed method much more accurately described the general nonlinear characteristics of acceleration distribution in the backfill soil under seismic conditions.

Additionally, for a given PGA, the acceleration distributions in the backfill soil varied for different seismic inputs along the depth. These variations were influenced by the spectral characteristics of different ground motions. For the spectra of the seismic inputs in the experiment, as illustrated in Fig. 13, the long-period contents of the Chichi wave were significantly more prominent than those of the other two waves. Thus, a stronger acceleration response was observed in the excited backfill soil for this particular scenario.

4.3. Results and discussions of seismic earth pressure

Acceleration time-history records from the sensor at the top of the near-model field were selected. The time instant when the acceleration reached its maximum peak value in the direction toward the bridge abutment model was aligned with $t = 0$ s moment in both the pseudo-dynamic method (with the initial phase taken as $\pi/2$) and the proposed modified method. The assumption served as the basis for the experimental comparative analysis of the theoretical models for deriving analytical solutions for seismic active earth pressure.

For all designed scenarios with different PGAs and seismic inputs, the comparison between the experimental data obtained using all three models and the theoretical solutions for the resultant force of seismic active earth pressure are shown in Table 4 and the intensity distributions are shown in Fig. 15.

Table 4
Comparison of resultant forces of seismic earth pressure.

PGA (*g*)	Methodology	Model 1 (kN/m)	Model 2 (kN/m)	Model 3 (kN/m)
0.1	Mean of experimental data	218	200	248
	Pseudo-static method	233	189	285
	Pseudo-dynamic method	220	177	271
	Proposed method	198	156	247
0.2	Mean of experimental data	164	152	194
	Pseudo-static method	287	240	343
	Pseudo-dynamic method	256	210	309
	Proposed method	200	158	249

As shown in Table 4, the results of the three analytical solutions were closely aligned, with small errors relative to the experimental data under low-PGA conditions. However, when the PGA increased to 0.2*g*, the proposed method significantly reduced the error in the resultant force relative to the experimental data, achieving an average error of 18.1 %, in contrast to those of the pseudo-static method (69.9 %) and pseudo-dynamic method (51.1 %).

Quantitative accuracy assessments of the errors between experimental and theoretical seismic earth pressure intensity distributions were conducted using two statistical metrics: root mean square error (RMSE) and mean absolute error (MAE). The results are systematically summarized in Table 5.

As shown in Fig. 15 and Table 5, at low PGA levels, the results from all three analytical solutions were close and the errors relative to the experimental data were all relatively small. However, as the PGA increased, the error between the theoretical models and the experimental data increased. The proposed modified method, which was based on an improved backfill soil seismic acceleration distribution assumption, better captured the nonlinear characteristics of the experimental seismic active earth pressure intensity distribution, demonstrating significantly reduced errors. Specifically, its RMSE decreased by 46.6 % and 30.3 % compared with those of the pseudo-static and pseudo-dynamic methods, respectively, and MAE decreased by 52.1 % and 33.0 % relative to the same methods. Notably, the conventional methods exhibited overly conservative results under a PGA of 0.2*g*, further highlighting the superior accuracy of the proposed approach in moderate seismic scenarios. In addition, the intensity distribution of seismic active earth pressure varied under different seismic inputs of the same PGA. Because of its high contents in the long-period range of the frequency domain, the earth pressure excited by the Chichi wave was greater than that of the El-Centro wave and the artificial wave.

5. Conclusions

This study developed an analytical method for calculating seismic active earth pressure for bridge abutments calibrated by a series of centrifuge model tests. The following conclusions were drawn.

- Using the amplitude characteristics of the design response spectrum sourced from the *Specifications for Seismic Design of Highway Bridges* of China and approximate mathematical relationships derived from the

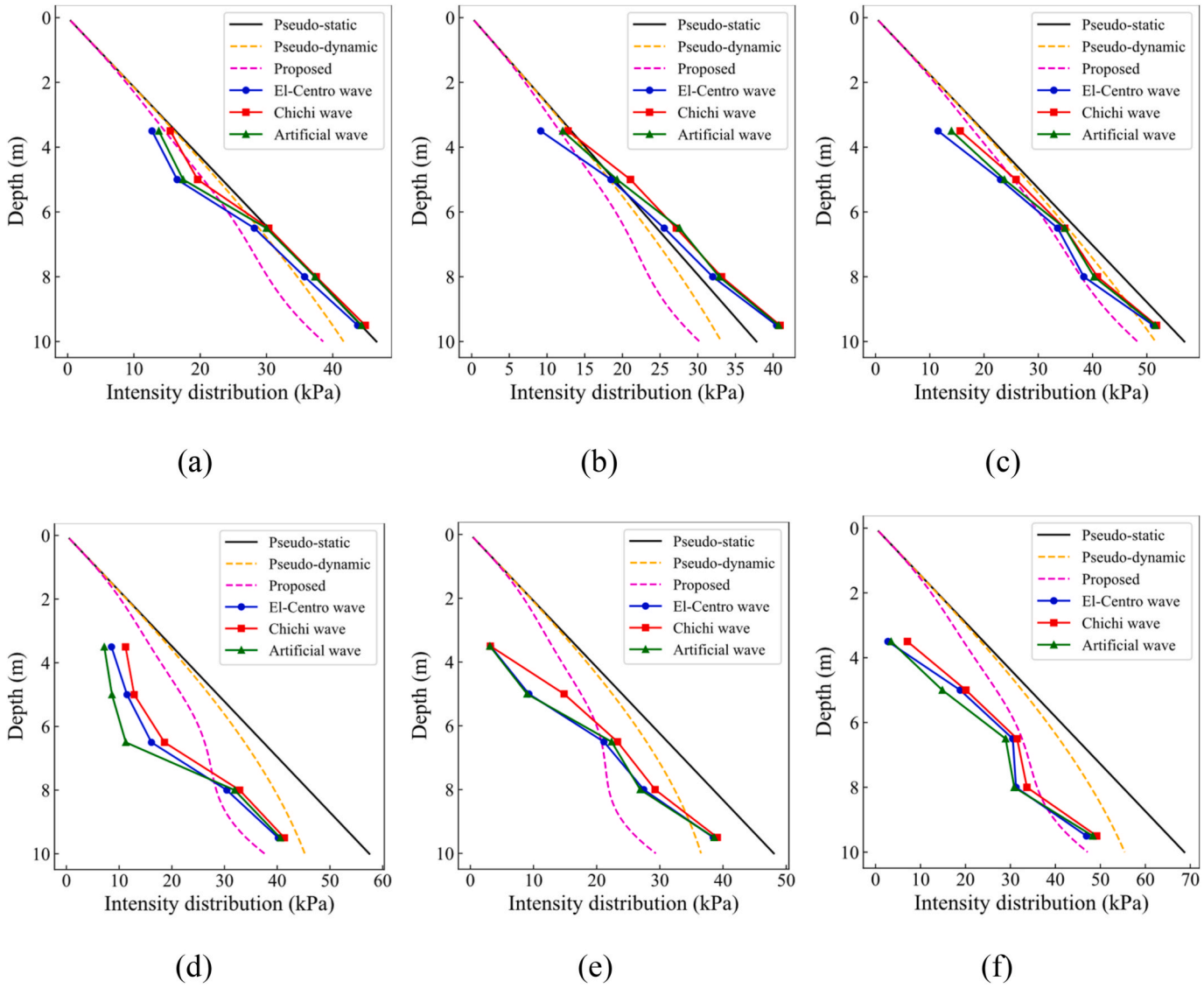

Fig. 15. Comparison of the intensity distributions of seismic earth pressure: (a) Model 1 at 0.1*g*, (b) Model 2 at 0.1*g*, (c) Model 3 at 0.1*g*, (d) Model 1 at 0.2*g*, (e) Model 2 at 0.2*g*, and (f) Model 3 at 0.2*g*.

Table 5
Mean values of the statistical metrics of different models and seismic inputs.

PGA (*g*)	Methodology	RMSE	MAE
0.1	Pseudo-static method	3.610	3.124
	Pseudo-dynamic method	4.022	3.408
	Proposed method	5.443	4.626
0.2	Pseudo-static method	15.77	15.42
	Pseudo-dynamic method	12.09	11.02
	Proposed method	8.429	7.386

Note: Each value in the table represents the arithmetic mean of error values of nine data points derived from the combination of all the abutment models and input ground motions.

random vibration theory along with Fourier transform, a detailed solution and a simplified solution for the horizontal seismic acceleration distribution in backfill soil for bridge abutments were derived.

- Based on the proposed simplified solution of seismic acceleration distribution and using the force and moment equilibrium equations of the sliding soil wedge in the limit equilibrium state, analytical formulas for the resultant force, intensity distribution, and resultant-force location of seismic active earth pressure for bridge abutments were derived. Parametric analyses were also conducted to clarify the major influence of key parameters on the proposed method.
- According to the analysis of centrifuge shaking table test results of bridge abutments scaled with a model similarity ratio of 50, higher PGA values led to higher nonlinearity in backfill soil seismic acceleration distribution and earth pressure intensity distribution on abutments. Through statistical metrics analyses, the modified method proposed herein was demonstrated to produce smaller errors and provided a more accurate characterization of nonlinear characteristics of seismic active earth pressure compared with conventional methods.

CRediT authorship contribution statement

Haoyu Xie: Writing – original draft, Methodology, Formal analysis, Data curation, Conceptualization. **Wengang Zhang:** Writing – review & editing, Supervision, Project administration, Data curation, Conceptualization. **Zhaoguang Tang:** Validation. **Chuan Wei:** Visualization. **Haiming Liu:** Resources.

Declaration of competing interest

The authors declare that they have no known competing financial interests or personal relationships that could have appeared to influence the work reported in this manuscript entitled "Seismic active earth pressure for bridge abutments based on design response spectrum".

Acknowledgments

This study was funded by the Natural Science Foundation of Chongqing CSTC [grant number CSTB2023NSCQ-MSX0775], the Chongqing Transport Technology Project [grant number CQJT-ZCXM2024-07], the Sichuan Transportation Science and Technology Project [grant number 2018-ZL-01], the National Natural Science Foundation of China [grant number 12032008], and the Fund of State Key Laboratory of Bridge Safety and Resilience [grant number 2024SKLBSR-DW005].

Appendix

Table A1
List of notations

Category	Symbol	Definition	Unit
Ground motion acceleration processing	$S(T)$	Acceleration response spectrum	m/s^2
	T	Period	s
	T_g	Characteristic period	s
	A	Peak ground motion acceleration	m/s^2
	$S_a(\omega)$	Power spectral density function	m^2/s^3
	ω	Angular frequency	rad/s
	$\Delta\omega$	Frequency interval	rad/s
	ω_{ch}	Characteristic angular frequency	rad/s
	ζ	Damping ratio	–
	D	Ground motion duration	s
	r	Exceedance probability	–
	$A_F(\omega_i)$	Discrete Fourier amplitude	m/s
	φ_i	Discrete phase angle	rad
	$a(t)$	Acceleration time history	m/s^2
	t	Time	s
	κ_i	Trigonometric coefficient	–
	k_i	Normalized trigonometric coefficient	–
Soil and structure property	H	Abutment height	m
	z	Depth	m
	v_s	Shear wave velocity	m/s
	G	Elastic modulus	Pa
	ρ	Density of soil	kg/m^3
	α	Abutment back angle	rad
	θ	Slip angle of soil wedge	rad
	δ	Abutment friction angle	rad
	φ	Soil friction angle	rad
Seismic earth pressure model	P_{ae}	Resultant seismic active earth pressure	N/m
	Q	Seismic inertial force	N/m
	W	Gravitational inertial force	N/m
	R	Resistance force	N/m
	p_{ae}	Seismic active earth pressure intensity	Pa
	H_d	Height of application point	m

Data availability

Data will be made available on request.

References

[1] Mononobe N. Considerations into earthquake vibrations and vibration theories. J Japan Soc Civil Eng 1924;10(5):1063–94.
[2] Okabe S. General theory on earth pressure and seismic stability of retaining wall. J Japan Soc Civil Eng 1924;10(6):1277–323.
[3] Steedman RS, Zeng X. The influence of phase on the calculation of pseudo-static earth pressure on a retaining wall. Geotechnique 1990;40(1):103–12.
[4] Seed HB, Whitman RV. Design of earth retaining structures for dynamic loads[C]. In: Proceedings of ASCE specialty conference on lateral stresses in the ground and design of earth-retaining structures, Ithaca; 1970. p. 103–47.
[5] Matsuo H. Experimental study on distributions of earth pressure acting on retaining walls during earthquakes. J Civil Eng Soc 1941;27(2):1–24.
[6] Matsuo H, Ohara S. Lateral earth pressure and stability of quay walls during earthquakes. Technol Rep Yamaguchi Univ 1976;1(4):455–66.
[7] Panah AK, Ramezani MS. Experimentally comparison of shaking table and pseudo-static parameters of polymeric-strip reinforced-soil walls. Jpn Geotech Soc Spec Publ 2024;10(43):1600–5.
[8] Wang YZ. Distribution of earth pressure on a retaining wall. Geotechnique 2000;50(1):83–8.
[9] Nouri H, Fakher A, Jones CJFP. Development of horizontal slice method for seismic stability analysis of reinforced slopes and walls. Geotext Geomembranes 2006;24(3):175–87.
[10] Nouri H, Fakher A, Jones CJFP. Evaluating the effects of the magnitude and amplification of pseudo-static acceleration on reinforced soil slopes and walls using the limit equilibrium horizontal slices method. Geotext Geomembranes 2008;26(3):263–78.
[11] Chandaluri VK, Sawant VA, Shukla SK. Seismic stability analysis of reinforced soil wall using horizontal slice method. Int J Geosynthe Ground Eng 2015;1:1–10.
[12] Lin YL, Leng WM, Yang GL, et al. Seismic active earth pressure of cohesive-frictional soil on retaining wall based on a slice analysis method. Soil Dynam Earthq Eng 2015;70:133–47.
[13] Farshidfar N, Keshavarz A, Mirhosseini SM. Pseudo-static seismic analysis of reinforced soil slopes using the horizontal slice method. Arabian J Geosci 2020;13:1–14.

[14] Morrison JrEE, Ebeling RM. Limit equilibrium computation of dynamic passive earth pressure. Can Geotech J 1995;32(3):481–7.
[15] Soubra AH. Static and seismic passive earth pressure coefficients on rigid retaining structures. Can Geotech J 2000;37(2):463–78.
[16] Veiskarami M, Chenari RJ, Jamee AA. A study on the static and seismic earth pressure problems in anisotropic granular media. Geotech Geol Eng 2019;37:1987–2005.
[17] Liu JY, Liu J. Seismic active earth pressure in nonhomogeneous and anisotropic soils. Comput Geotech 2024;170:106315.
[18] Alhajj Chehade H, Dias D, Sadek M, et al. Pseudo-static analysis of reinforced earth retaining walls. Acta Geotechnica 2021;16:2275–89.
[19] Pantelidis L. The generalized coefficients of earth pressure: a unified approach. Appl Sci 2019;9(24):5291.
[20] Le CV, Ho VQ, Ho PLH, et al. Limit state analysis of thin plates and slabs by a numerical pseudo-lower yield design approach. Thin-Walled Struct 2022;172:108852.
[21] Chen FQ, Chen C, Kang WZ, et al. Slip-line solution to seismic active earth pressure of narrow c-φ soils on gravity walls rotating about the bottom. Soil Dynam Earthq Eng 2024;181:108625.
[22] Zeng X, Steedman RS. On the behaviour of quay walls in earthquakes. Geotechnique 1993;43(3):417–31.
[23] Azad A, Yasrobi SS, Pak A. Seismic active pressure distribution history behind rigid retaining walls. Soil Dynam Earthq Eng 2008;28(5):365–75.
[24] Ghosh S, Sharma RP. Pseudo-dynamic active response of non-vertical retaining wall supporting c-Φ backfill. Geotech Geol Eng 2010;28:633–41.
[25] Zhang ZL, Yang XL. Seismic stability analysis of slopes with cracks in unsaturated soils using pseudo-dynamic approach. Transport Geotech 2021;29:100583.
[26] Basha BM, Babu GLS. Computation of sliding displacements of bridge abutments by pseudo-dynamic method. Soil Dynam Earthq Eng 2009;29(1):103–20.
[27] Pain A, Choudhury D, Bhattacharyya SK. Seismic stability of retaining wall-soil sliding interaction using modified pseudo-dynamic method. Géotech Lett 2015;5(1):56–61.
[28] Nimbalkar S, Choudhury D. Sliding stability and seismic design of retaining wall by pseudo-dynamic method for passive case. Soil Dynam Earthq Eng 2007;27(6):497–505.
[29] Giri D, Bandopadhyay A. Influence of soil amplification and backfill angle on seismic earth pressure coefficients by pseudo dynamic method. Geomechanics Geoengin 2022;17(6):2005–12.
[30] Fathipour H, Siahmazgi AS, Payan M, et al. Evaluation of the active and passive pseudo-dynamic earth pressures using finite element limit analysis and second-order cone programming. Geotech Geol Eng 2023;41:1921–36.
[31] Halder K, Chakraborty D. Estimation of seismic active earth pressure on reinforced retaining wall using lower bound limit analysis and modified pseudo-dynamic method. Geotext Geomembranes 2023;51(1):100–16.
[32] Lei M, Li J, Zhao C, et al. Pseudo-dynamic analysis of three-dimensional active earth pressures in cohesive backfills with cracks. Soil Dynam Earthq Eng 2021;150:106917.
[33] Kumar M, Chatterjee K. Modified pseudo-dynamic based soil-structure interaction of caisson with a novel 3D failure wedge. Comput Geotech 2023;153:105079.
[34] Ministry of Transport of the People's Republic of China. Specifications for seismic design of highway bridges: JTG/t 2231-01-2020[S]. Beijing: China Communications Press; 2020 (in Chinese).
[35] Vanmarcke EH. Properties of spectral moments with applications to random vibration. J Eng Mech Div 1972;98(2):425–46.
[36] Kaul MK. Stochastic characterization of earthquakes through their response spectrum. Earthq Eng Struct Dynam 1978;6(5):497–509.
[37] Park YJ. New conversion method from response spectrum to PSD functions. J Eng Mech 1995;121(12):1391–2.
[38] Cacciola P. A stochastic approach for generating spectrum compatible fully nonstationary earthquakes. Comput Struct 2010;88(15–16):889–901.
[39] Nie JR. Exploration of the effects of response spectrum matching on power spectral density functions[C]. In: Proceeding of ASME 2024 pressure vessels and piping conference, USA; 2024. V005T08A024.
[40] Shang Q, Li J, Wang T. Floor acceleration response spectra of elastic reinforced concrete frames. J Build Eng 2022;45:103558.
[41] Tong L, Wang D, Sun Z, et al. Seismic uplift effect at end spans of long-span rigid-frame bridges subjected to near-fault and far-fault ground motions. J Bridge Eng 2023;28(7):05023001.
[42] Zhang ZH, Li QS. Seismic responses of super high-rise buildings under long-period ground motions. Eng Struct 2023;294:116824.
[43] Ministry of Housing and Urban-Rural Development of the People's Republic of China. Code for seismic design of urban bridges: CJJ 166-2011[S]. Beijing: China Architecture & Building Press; 2011 (in Chinese).
[44] Widuliński Ł, Tejchman J, Kozicki J, et al. Discrete simulations of shear zone patterning in sand in earth pressure problems of a retaining wall. Int J Solid Struct 2011;48(7–8):1191–209.